



A family of polyoxometalate-resorcin[4]arene-based metal–organic materials: Assemblies, structures and lithium ion battery properties



Ming-Yue Yu¹, Jin-Hua Liu¹, Jin Yang*, Jian-Fang Ma*

Key Lab for Polyoxometalate Science, Department of Chemistry, Northeast Normal University, Changchun 130024, China

ARTICLE INFO

Article history:

Received 12 November 2020

Received in revised form 7 January 2021

Accepted 30 January 2021

Available online 10 February 2021

Keywords:

Polyoxometalate

Resorcin[4]arene

Crystal structure

Lithium-ion batteries

ABSTRACT

Polyoxometalates (POMs) are alternative anode materials of lithium ion batteries (LIBs) for their reversible electrochemical redox behaviors and electron storage functions. To overcome the low conductivity and poor stability of the POMs, embedment of POMs into metal–organic hybrid complexes is a promising synthetic strategy. Here, we designed a family of copper-containing POM-resorcin[4]arene-based complexes supported by a resorcin[4]arene ligand (TPTR4A), copper cations and Keggin-type POMs, namely, $[\text{Cu}_4(\text{TPTR4A})_2][\text{PMo}_{12}\text{O}_{40}](\text{OH})\cdot2\text{DMA}\cdot\text{H}_2\text{O}$ (**1a**), $[\text{Cu}_4(\text{TPTR4A})_2][\text{SiW}_{12}\text{O}_{40}]\cdot2.5\text{DMA}$ (**1b**) and $[\text{Cu}_4(\text{TPTR4A})_2][\text{PW}_{12}\text{O}_{40}](\text{OH})\cdot0.5\text{DMA}\cdot5\text{H}_2\text{O}$ (**1c**) (DMA = *N,N*-dimethylacetamide). To improve the conductivity of the complexes, composites **1a@GO-1c@GO** were obtained through mechanical grinding of the complexes and graphene oxide (GO). Strikingly, they show high initial specific capacity and stability for LIBs. This work offered a strategy for application of the POM-based complexes as LIBs via combining POM-based complexes and RGO.

© 2021 Elsevier B.V. All rights reserved.

1. Introduction

Lithium ion batteries (LIBs) have gained considerable attention owing to their potential application in energy storage systems [1–5]. In this aspect, traditional graphites, as the most common commercial electrode materials, impede their development in LIBs due to the limited theoretical capacity [6–10]. Thus, the exploration of new electrode materials has become a hotspot for energy storage. Polyoxometalates (POMs), a class of nanoscale metal-oxo clusters, are ideal candidates for anode materials of LIBs owing to their attractive physical and chemical properties [11–17], including tunable compositions, electron storage functions and reversible electrochemical redox behaviors [18,19]. Nevertheless, poor conductivity and instability in electrolyte hinder their further development as anode materials [20–23]. Self-assembly of POMs and proper substrates to form POM-based hybrid complexes is a promising synthetic approach owing to the structural diversity and increased stability of the resulting materials [15,20,24–31].

In this facet, functionalized calix[4]arenes are potential macrocyclic ligands for constructing inorganic–organic complexes [32–37]. Particularly, the functionalized calix[4]arenes with multi-chelating

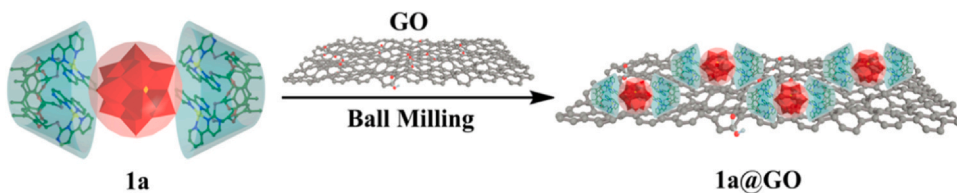
groups are excellent candidate ligands for this purpose [38,39]. Thus, the proper combination of POMs with calix[4]arenes will produce inorganic–organic complexes with tunable structures, high stability and potential applications [40–42]. However, the examples that POM-calixarene-based hybrid complexes applied in LIBs have been rarely reported [5,43].

In this work, we synthesized a new resorcin[4]arene-based ligand with four chelating 4-(pyridin-2-yl)pyrimidine-2-thiolate groups (TPTR4A) (Scheme 1). The multidentate TPTR4A ligand is easy to chelate with metal ions to generate attractive structures and improved stability of the obtained complexes [5,43]. In this work, a family of stable POM-resorcin[4]arene-based complexes, namely, $[\text{Cu}_4(\text{TPTR4A})_2][\text{PMo}_{12}\text{O}_{40}](\text{OH})\cdot2\text{DMA}\cdot\text{H}_2\text{O}$ (**1a**), $[\text{Cu}_4(\text{TPTR4A})_2][\text{SiW}_{12}\text{O}_{40}]\cdot2.5\text{DMA}$ (**1b**) and $[\text{Cu}_4(\text{TPTR4A})_2][\text{PW}_{12}\text{O}_{40}](\text{OH})\cdot0.5\text{DMA}\cdot5\text{H}_2\text{O}$ (**1c**) (DMA = *N,N*-dimethylacetamide), were achieved by assembly of TPTR4A, copper cations and Keggin-type POMs. To improve the conductivity and capacity of these complexes, such POM-resorcin[4]arene-based materials were anchored to the surface of reduced graphene oxide (RGO) through mechanical grinding of the complexes and graphene oxide (**Cu-POMs@GO**, Scheme 2) [44–50]. As a consequence, the resulting composites show much better electrochemical behaviors than the POM-resorcin[4]arene-based complexes.

* Corresponding authors.

E-mail addresses: yangj808@nenu.edu.cn (J. Yang), majf247@nenu.edu.cn (J.-F. Ma).

¹ These authors contributed equally to this work.

**Scheme 1.** Synthetic scheme of TPTR4A ligand.**Scheme 2.** Synthetic route of **1a@GO**.

2. Results and discussion

2.1. Structural description

SQUEEZE routine was used for removing the disordered solvents in the refinement of the compounds [51]. The number of the solvents was proved with thermogravimetric analysis (TG), electron diffraction density and elemental analysis (Fig. S1) [41]. The oxidation states of molybdenum atoms, tungsten atoms, copper atoms in the compounds were verified via X-ray photoelectron spectroscopy (XPS) (Figs. S2–S6).

2.1.1. Structural description of (1a)–(1c)

Single-crystal XRD reveals that **1a**–**1c** crystallized in the triclinic system with space group *P*-1. The structures of **1b** and **1c** are similar to that of **1a** except that the anions are replaced by $[\text{SiW}_{12}\text{O}_{40}]^{4-}$ and $[\text{PW}_{12}\text{O}_{40}]^{3-}$ anions, respectively, (Figs. 1, S7 and S8). In **1a**, the asymmetric unit contains one TPTR4A ligand, two Cu(I) cations, half of a $[\text{PMo}_{12}\text{O}_{40}]^{3-}$ anion, and half of a free OH^- anion. Two Cu(I) cations (Cu1 and Cu2) adopt the same four-coordinated mode: each Cu(I) cation is coordinated with four N atoms (N1, N3, N10 and N12 for Cu1 ; N4, N6, N7 and N9 for Cu2) (Fig. 2a). The Cu(I)–N distances are in the range of 1.975(7)–2.063(7) Å (Table S1). Two $[\text{Cu}_2(\text{TPTR4A})_2]^{2+}$ units are linked by a $[\text{PMo}_{12}\text{O}_{40}]^{3-}$ anion to form a $[\text{Cu}_4(\text{TPTR4A})_2(\text{PMo}_{12}\text{O}_{40})]^+$ unit via the weak C–H···O hydrogen bonds (Fig. 2b). Further, adjacent $[\text{Cu}_4(\text{TPTR4A})_2(\text{PMo}_{12}\text{O}_{40})]^+$ units were linked via C–H···O interactions to form 1D supramolecular chains (Table S2), as shown in Fig. 2c and d.

2.2. Physical characterization

POM-resorcin[4]arene-based complexes **1a**–**1c** are stable in electrolyte (Fig. 3a–c). Evidently, POMs with redox behaviors act as a key role in stabilizing the structures of complexes during their construction. The composites of **1a@GO**–**1c@GO** were obtained by

ball-milling of **1a**–**1c** with GO, respectively. Powder X-ray diffraction (PXRD) of each composite is consistent with the simulated one, demonstrating that the mechanical grinding does not change the structure of the **Cu-POMs** system (Fig. 3) [47,52,53]. FT-IR spectra of **1a**–**1c** also correspond to those of **1a@GO**–**1c@GO**. For example, both **1a** and **1a@GO** show the characteristic peaks at 1059, 962, 876 and 811 cm⁻¹, which are assigned to P–O and Mo–O vibrations of $[\text{PMo}_{12}\text{O}_{40}]^{3-}$ anions [40]. Besides, the characteristic peaks at 971, 922, 884 and 804 cm⁻¹ for **1b**/**1b@GO** and 1080, 977 and 891 cm⁻¹ for **1c**/**1c@GO** correspond to $[\text{SiW}_{12}\text{O}_{40}]^{4-}$ (Si–O and W–O) and $[\text{PW}_{12}\text{O}_{40}]^{3-}$ (P–O and W–O), respectively [27,40]. The bands in the range of 2973–1212 cm⁻¹ for **Cu-POMs** and **Cu-POMs@GO** belong to the characteristic peaks of ligand TPTR4A (Fig. S9). Particularly, the characteristic peaks of functional groups from RGO were almost covered by the sharp peaks of **Cu-POMs** after the **Cu-POMs** incorporation into RGO [54], demonstrating the successful preparation of **Cu-POMs@GO**.

As illustrated in Fig. 4, N_2 adsorption isotherms for **1a** and **1a@GO** were determined. For **1a**, the Brunauer–Emmett–Teller (BET) value is 57.998 m² g⁻¹ and the average pore diameter is 1.007 nm. The corresponding ones of **1a@GO** were enhanced to 169.551 m² g⁻¹ and 3.385 nm, respectively [55,56]. The result may account for **Cu-POM** incorporation into RGO, which increased contact areas between the electrolyte and the composite. Similarly, for **1b@GO** and **1c@GO**, the BET surface areas are 115.559 and 124.367 m² g⁻¹, respectively (Fig. S10).

Scanning electron microscope (SEM) and transmission electron microscopy (TEM) images of **Cu-POMs** and **Cu-POMs@GO** are illustrated in Fig. 5. It is clear that complexes **Cu-POMs** are visible with a crystalline phase of diamond-shaped lamellar crystals (Fig. 5a–c). The species of **Cu-POMs** are well-dispersed on RGO based on the SEMs and TEMs of **Cu-POMs@GO** (Fig. 5d–i). The result further demonstrated the successful combination of RGO and **Cu-POMs** after ball milling, which may account for the improvement of the

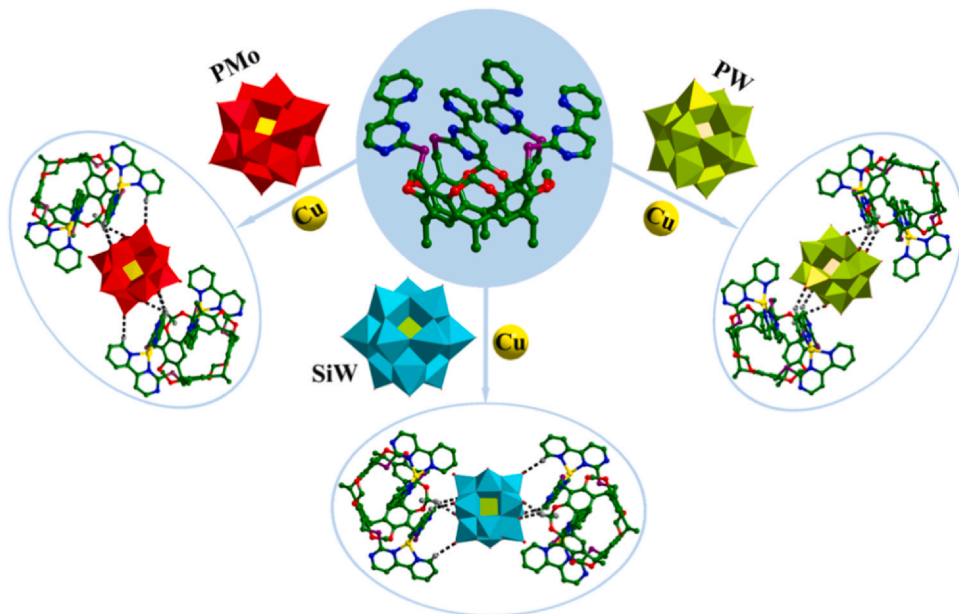


Fig. 1. Schematic representation of the synthetic strategy for **1a–1c**.

conductivity of the resulting composites. Obviously, the reduced sizes were achieved after ball milling (Fig. S11), resulting in the enlarged BET surface areas and exposed active sites. Thus, it is easy for Li^+ to contact with active sites. The mapping analysis of each element was collected from the designated area (Figs. 6, S12 and S13, revealing that the uniform distribution of these elements within composites **Cu-POMs@GO**.

2.3. Electrochemical performance

Inspired by the outstanding electrochemical behaviors of the POM-based materials, the potential application of **1a@GO-1c@GO**

was explored as electrode materials for LIBs. As shown in Fig. 7, the cyclic voltammogram (CV) curves of **Cu-POMs** and **Cu-POMs@GO** were recorded from 0.01 to 3 V. For these materials, the irreversible reduction peak was observed between 0.6 and 0.8 V in the first cycle, which was from the production of the solid electrolyte interphase (SEI) film and the electrolyte decomposition [57,58]. The reduction peaks at ~1.6 V for **Cu-POMs** and ~1.7 V for **Cu-POMs@GO** may be ascribed to the first process of the inserting Li^+ ions [59,60]. In addition, for **1a@GO**, a pair of reversible redox peaks were observed at 1.42 V (the oxidation) and 1.30 V (the reduction) in the first cycle, demonstrating a defined electrochemical process, which accounted for the reduction and oxidation of Mo^{6+} [5,46]. Meanwhile, the

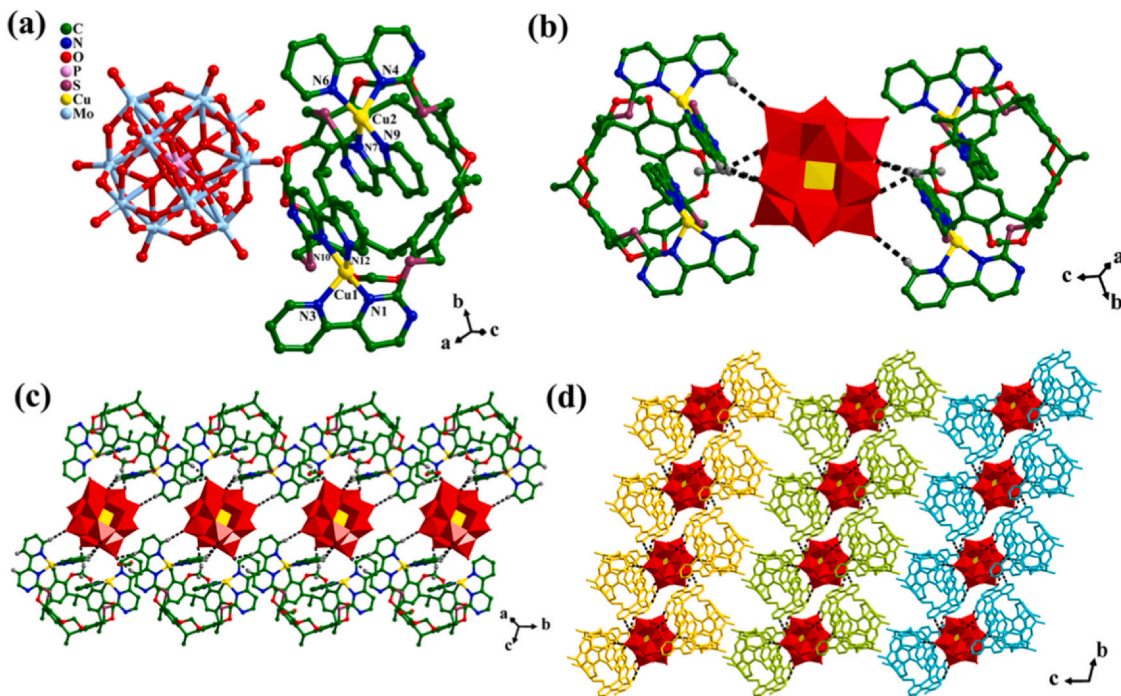


Fig. 2. (a) Coordination environments of $\text{Cu}(\text{I})$ cations in **1a**. (b) View of the $[\text{Cu}_4(\text{TPTR4A})_2(\text{PMo}_{12}\text{O}_{40})]^{+}$ unit formed with the weak $\text{C}-\text{H}\cdots\text{O}$ interactions. (c) and (d) view of the supramolecular chains formed by the weak $\text{C}-\text{H}\cdots\text{O}$ interactions.

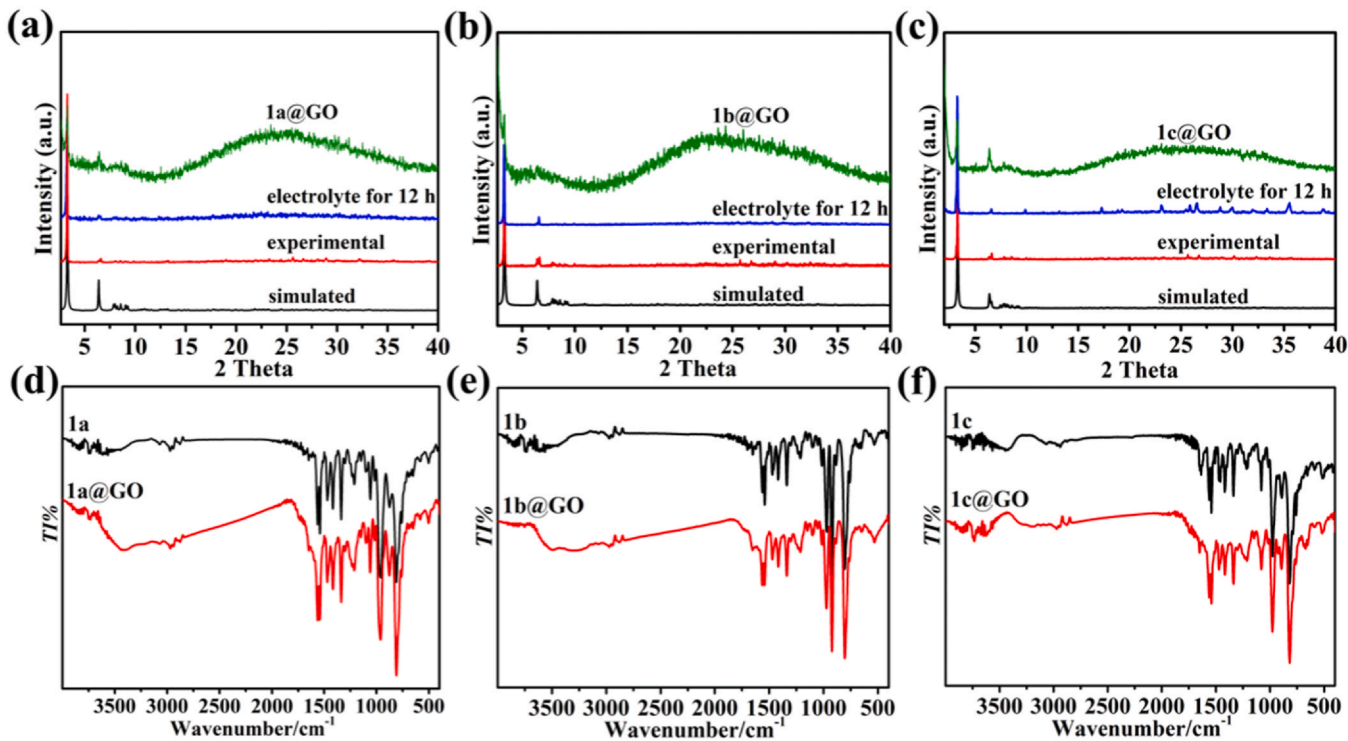


Fig. 3. PXRD patterns of **1a–1c** for the simulated, the as-synthesized, the sample soaked in electrolyte and the ones combined with GO (a–c). FT-IR spectra for the as-synthesized **1a–1c** and the combined with GO (d–f).

reversible redox peak pairs were also found for **1b@GO** and **1c@GO**, respectively, which may be attributed to the reduction and oxidation of W⁶⁺ [12]. Noticeably, the subsequent CV curves were almost overlapped, revealing the good electrochemical stability of **Cu-POMs@GO** composites. Moreover, the CV curves of **Cu-POMs@GO** were similar to those of **Cu-POMs**, demonstrating that the electrochemical mechanism is not changed.

As illustrated in Fig. S14, the initial discharge/charge capacities of **1a–1c** were only 812/220, 1066/236 and 592/154 mA h g⁻¹, respectively. By contrast, **1a@GO-1c@GO** displayed the initial discharge/charge capacities of 1506/862, 1771/1035 and 1380/798 mA h g⁻¹, respectively. The corresponding coulombic efficiencies (CE) are 57%, 58% and 58%, respectively. Clearly, these CE values were much higher than those of **1a** (27%), **1b** (22%) and **1c** (26%) (Fig. 8). The obvious capacity

loss for these materials was probably ascribed to the generation of the SEI films [52,58,61]. At the same time, the galvanostatic charge-discharge (GCD) curves were overlapped for the second and the third cycles, indicating the good recycling stability. In addition, these materials displayed obvious plateaus. For example, the GCD curves of **1a@GO** showed three plateaus at 1.67, 1.33 and 0.75 V, which corresponded to the results of CVs. Particularly, **Cu-POMs@GO** composites exhibited much higher reversible capacities than those of **Cu-POMs** in the whole recycling process, in which the high reversible discharge capacities (836, 947 and 888 mA h g⁻¹ for **1a@GO-1c@GO**, respectively) with the high CE of 99% were achieved after 100 cycles (Fig. 8).

In view of the remarkable electrochemical performance of the **Cu-POMs@GO** composites at 0.1 A g⁻¹, the recycling stability and practical applications of the composites were further investigated at

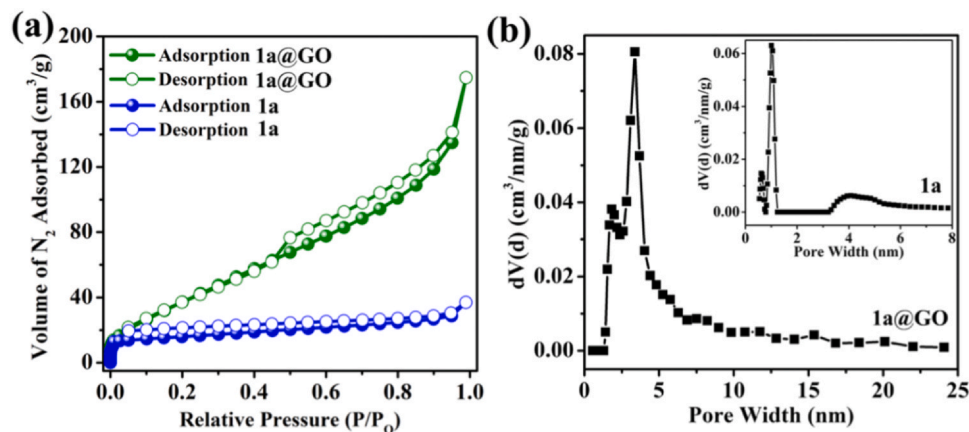


Fig. 4. N₂ adsorption isotherms (a) and pore size distributions (b) for **1a@GO** and **1a**.

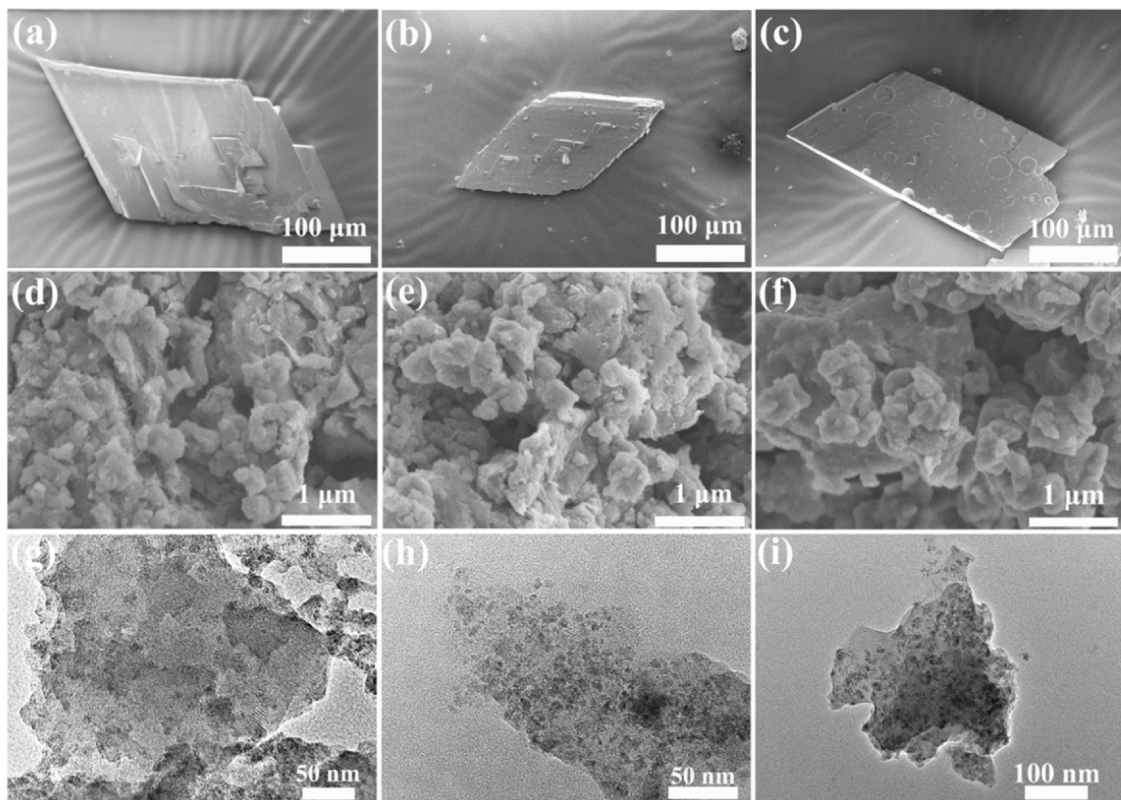


Fig. 5. SEMs of **1a–1c** (a–c), **1a@GO–1c@GO** (d–f) and TEMs of **1a@GO–1c@GO** (g–i), respectively.

0.1–5 A g⁻¹ (Fig. 9, Table S3). For instance, the discharge capacities for **1a@GO** were ca. 805, 756, 698, 626, 596, 496, 376 and 326 mA h g⁻¹ at 0.1–5 A g⁻¹, respectively (Fig. 9a). The capacity (840 mA h g⁻¹) was still retained at 0.1 A g⁻¹, verifying the composite possessed high stability. Remarkably, compared with **1a**, **1a@GO** possessed the superior rate performance, demonstrating that RGO acted as a key role in improving the conductivity of the resulting composites [44–50]. Evidently, the discharge capacity of **1a@GO** was better than the known CPR/rGO composites (790 mA h g⁻¹) at 0.1 A g⁻¹ [62]. The electrochemical performance of **1a@GO** was compared to other

POM-based materials (Table S4). In addition, electrochemical impedance spectroscopies (EISs) were determined to discuss the electrochemical processes of these electrodes. R1 represented the electrodes and electrolyte resistance. The Nyquist plots of composites **Cu-POMs@GO** showed smaller semicircles at high-frequency region than those **Cu-POMs** (Fig. 9d–f), indicating that the **Cu-POMs@GO** electrodes possessed the low internal resistance (R2 and R3) [63]. Meanwhile, the large slopes were observed for **Cu-POMs@GO** in the region of the low frequency, which showed the low ion diffusion resistance (W₀). The result revealed that the

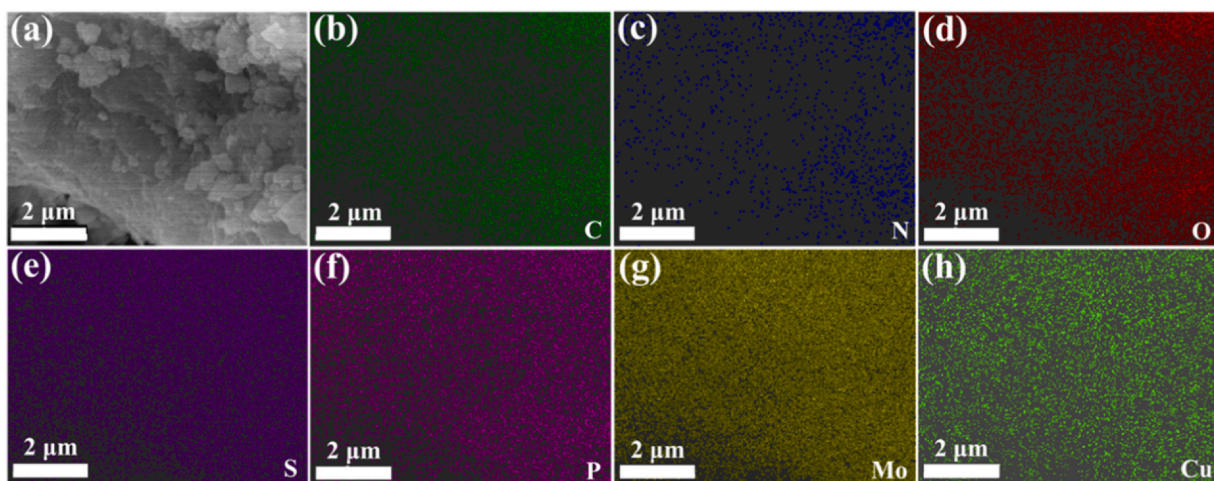
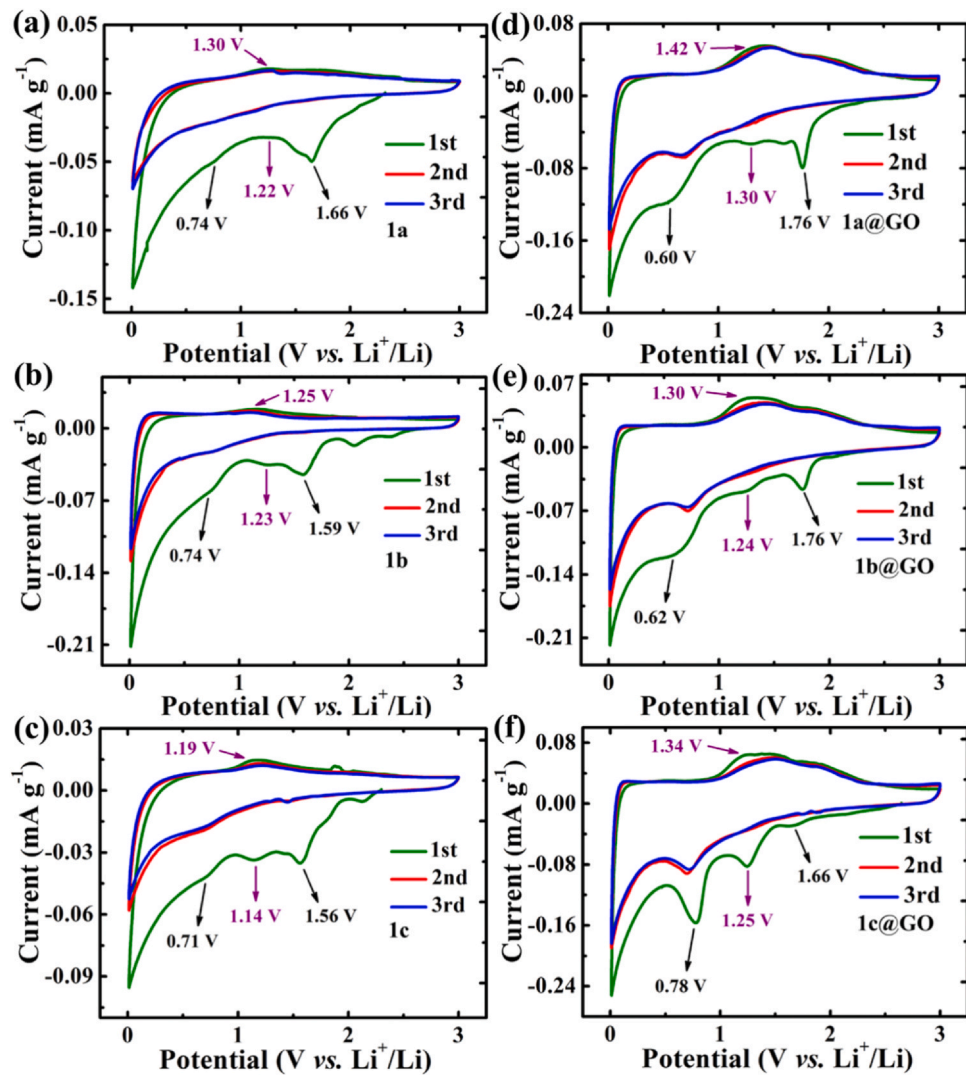


Fig. 6. Elemental mapping images of **1a@GO**.

Fig. 7. CV curves of **1a–1c** (a–c) and **1a@GO-1c@GO** (d–f) at 0.01–3 V.

combination of **Cu-POMs** and RGO not only resulted in fast charge transfer and Li^+ migration, but also highly improved the electrochemical properties of the resulting composites.

Moreover, the **1a@GO//NCM111-1c@GO//NCM111** full-cells were assembled to evaluate the practical applications of these materials (Figs. S15 and S16). Fig. 10a showed the GCD curves of NCM111 and **1a@GO** at 100 mA g^{-1} in the half cell. The GCD curves of the **1a@GO//NCM111** full-cell from 1.2 to 4.5 V were depicted in Fig. 10b. The charge and discharge capacities for the first cycle were 203 and 165 mA h g^{-1} , respectively, and the initial CE value was up to 81.3%. For the cycling performance, a high discharge capacity of 92 mA h g^{-1} was achieved at 100 mA g^{-1} (Fig. 10c), and the capacity retention reached to 55.8% after 100 cycles.

To further evaluated the reaction mechanism of LIBs, the chemical composition and element valence of **Cu-POMs** before and after discharge at 0.01 V were measured with the XPS measurements (Figs. 11, S2 and S3). As illustrated in Fig. 11a, **1a** contained C, N, O, S, P, Mo and Cu elements, and **1b** and **1c** possessed C, N, O, S, Si, W, Cu elements and C, N, O, S, P, W, Cu elements, respectively (Figs. S2a and S3a). For the C 1s spectrum of **1a**, there exist four peaks associated with C=O (288.4 eV), C–O (286.8 eV), C–N (285.5 eV) and C–C

(284.5 eV) (Fig. 11b) [64,65]. After discharge at 0.01 V, the C=O peak became clear because of the intercalation of Li^+ and the formation of SEI films (the main composite was Li_2CO_3) (Fig. 11e) [20]. The similar phenomenon was also observed for **1b** and **1c** (Figs. S2e and S3e). In addition, the Mo 3d spectrum of **1a** before test showed two main peaks at the banding energy of 232.0 eV and 235.1 eV, corresponding to $\text{Mo}^{\text{VI}}3\text{d}_{5/2}$ and $\text{Mo}^{\text{VI}}3\text{d}_{3/2}$ (Fig. 11c) [18]. After discharge at 0.01 V, part of Mo^{VI} was reduced to Mo^{V} due to the appearance of Mo^{V} peaks at 231.4 eV and 234.7 eV (Fig. 11f) [66,67]. Meanwhile, in respect to the original W^{VI} oxidation state, the XPS signals of partially reduced W^{V} appeared at 35.1 eV ($\text{W} 4\text{f}_{7/2}$) and 37.2 eV ($\text{W} 4\text{f}_{7/2}$) for **1b**, and at 35.1 eV ($\text{W} 4\text{f}_{7/2}$) and 37.3 eV ($\text{W} 4\text{f}_{7/2}$) for **1c**, respectively, after discharge at 0.01 V (Figs. S2f and S3f) [68]. The result further proved that the redox reactions occurred in lithium-ion batteries. Moreover, Cu 2p spectrum of **1a** possessed two main peaks of Cu 2p_{3/2} (931.8 eV) and Cu 2p_{1/2} (951.7 eV), demonstrating the presence of Cu^+ (Fig. S17a) [69]. Also, there existed two peaks at 933.4 eV and 953.6 eV, which may be assigned to $\text{Cu}^{2+} 2\text{p}_{3/2}$ and $\text{Cu}^{2+} 2\text{p}_{1/2}$ derived from the oxidation of Cu^+ by O_2 in air, respectively [69,70]. The ratios of $\text{Cu}^+/\text{Cu}^{2+}$ of **1a–1c** were almost unchanged after discharge, demonstrating that copper did not participate in the electrochemical

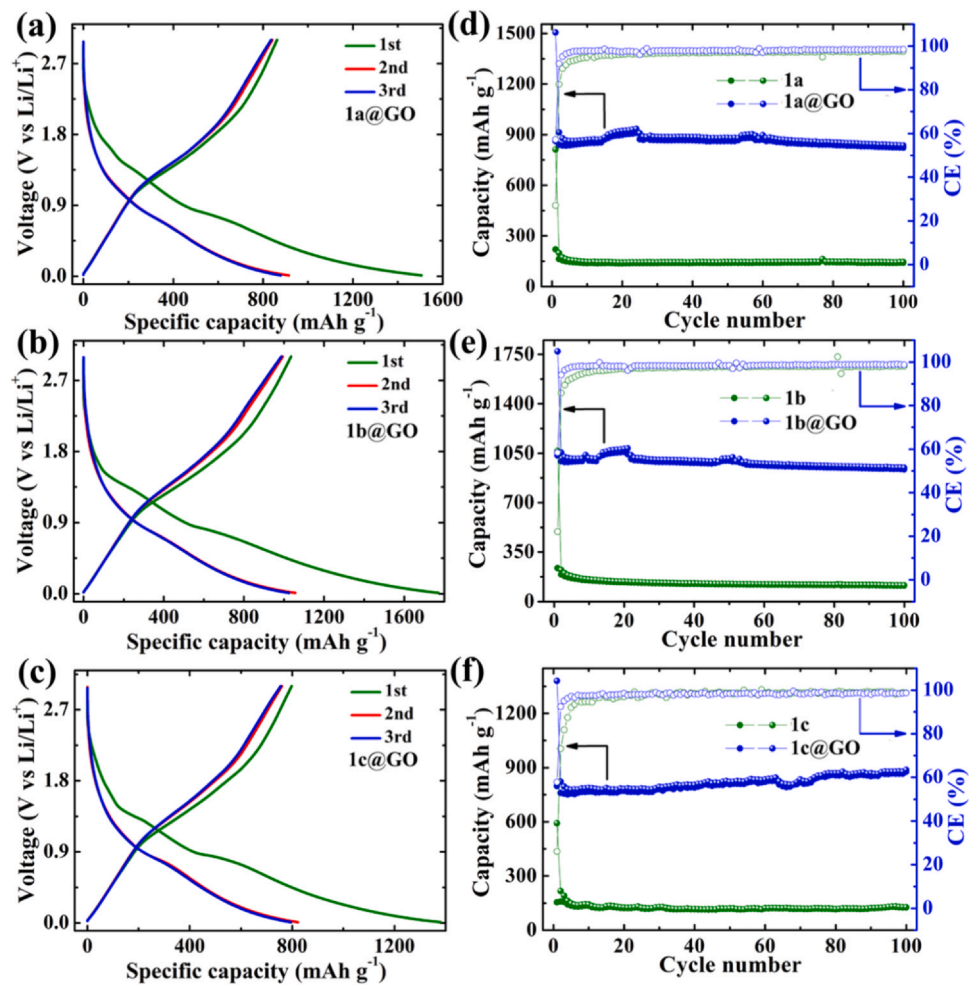


Fig. 8. GCD curves of **1a@GO-1c@GO** (a–c) from 0.01 to 3 V. Cycling capacity and CE of **1a-1c** and **1a@GO-1c@GO** (d–f) at 0.1 A g⁻¹.

reactions (Fig. S17d). Ex-situ PXRD patterns of **1a-1c** after the first cycle were determined to explore the impressive reversibility. The results showed that the peak intensities of **1a-1c** reduced after the insertion of lithium ions, indicating that the crystallization of **1a-1c** became weak [12]. Nevertheless, the structures of **1a-1c** could still retain after the first cycle (recharged to 3.0 V), indicating that these materials could endure the volume variation with structural integrity after undergoing the redox reaction (Fig. 12), which ensured the excellent capacity retention.

In view of the results of XPS and ex-situ XRD, the electrochemical redox process mainly occurred on the Mo and W species in POMs, and these materials can endure the volume variation with structural integrity after undergoing the redox reaction. The results established a specific lithium storage mechanism for the **Cu-POMs@GO** composites.

Based on our experiments and the XPS results, the possible reason for the enhanced electrochemical performance of **Cu-POMs@GO** composites was discussed. In this respect, the Li⁺ storage mechanism of **Cu-POMs@GO** composites may account for the synergistic effects of **Cu-POMs** and RGO. First, the combination of resorcin[4]arene and POMs improved the stability of **Cu-POMs** [35–37], thus affording a prerequisite for their application as anode materials of LIBs. Second, the high density of the exposed O sites on POMs led to the increased Li⁺ storage capacity [15]. The valence

changes of Mo and W (from Mo⁶⁺ to Mo⁵⁺ and from W⁶⁺ to W⁵⁺) calculated with XPS confirms that the redox reactions occurred between POMs and Li⁺ after discharge at 0.01 V [67]. Third, the un-coordinated N atoms from ligand TPTR4A in **Cu-POMs** maybe capture the Li⁺ ions and participate in Li insertion, which was in favor of storing Li⁺ ions and generating excellent electrochemical performance [20]. Finally, the combination with RGO not only improved the conductivity of **Cu-POMs**, but also made full use of the advantage of the small sizes and large surface areas of the resulting composites, thus realizing to full contact with electrolyte [44–50].

To certify whether the capacity is dominated by the capacitive behaviors or not, the CVs of **Cu-POMs@GO** with different scan rates (0.1–5 mV/s) were recorded from 0.01 to 3.0 V (Figs. 13a, S18a and S19a). Further, the power law $i = av^b$ was used to explore the electrode reaction types (i , v , a and b are the peak current, scan rate and alterable parameters, respectively). Generally, the b value of 0.5 reveals a diffusion-controlled process, whereas the b value of 1 means the reaction being capacitive-controlled [20]. For **1a@GO-1c@GO**, the b values for anodic peaks were 0.77, 0.78, and 0.81, respectively, demonstrating that their electrochemical behaviors are mainly capacitive process (Figs. 13b, S18b and S19b). Based on $i = k_1v + k_2v^{0.5}$ (k_1 and k_2 represented the surface capacitive- and diffusion-controlled contributions, respectively) [46], 66%, 72% and 77% of the capacitance-contributions at 5 mV/s were achieved for **1a@GO-**

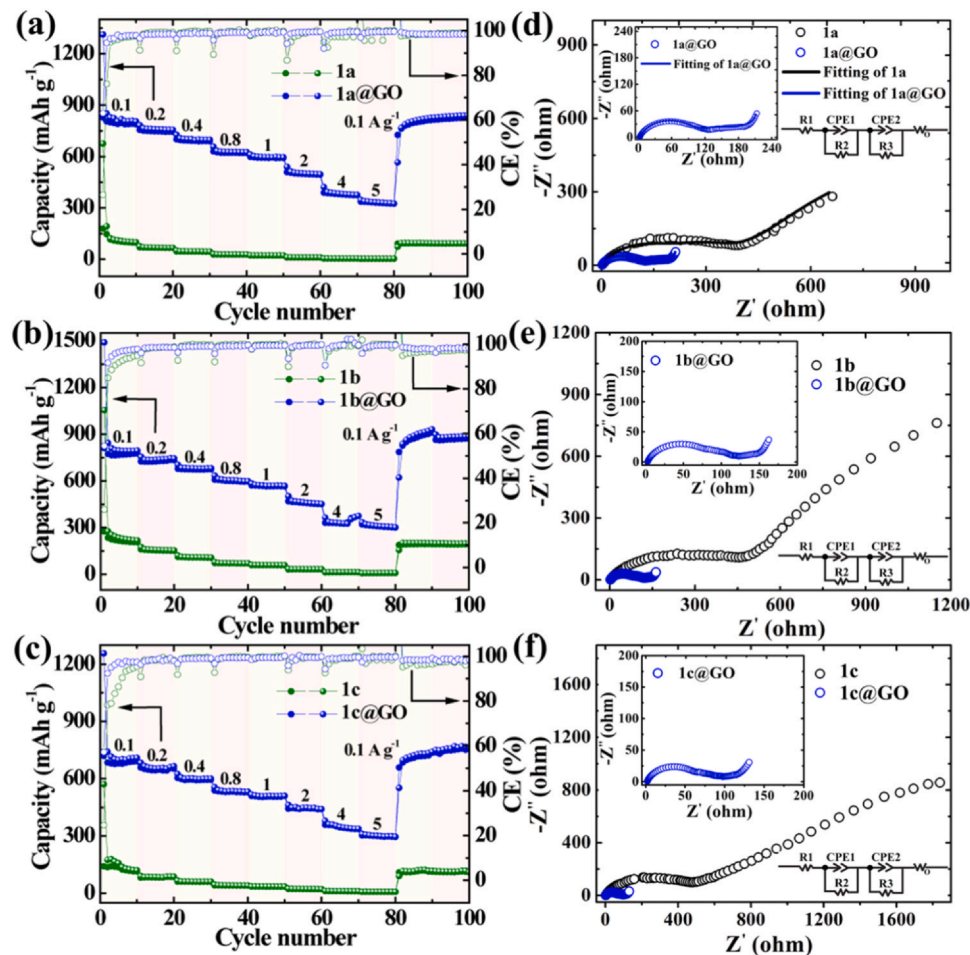


Fig. 9. Rate capability comparison of **1a–1c** and **1a@GO–1c@GO** (a–c) at 0.1 A g⁻¹ and 5 A g⁻¹. EIS plots of **1a–1c** and **1a@GO–1c@GO** (d–f) anodes.

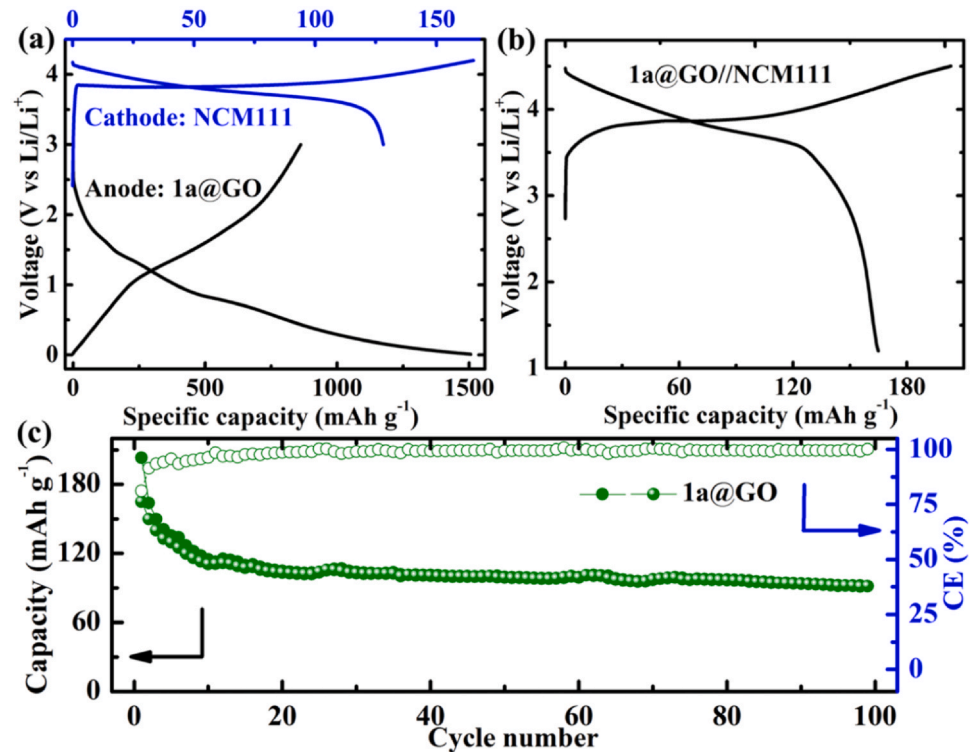


Fig. 10. Electrochemical performance of the **1a@GO//NCM111** full-cell. (a) Charge-discharge curves of NCM111 and **1a@GO** in the Li⁺ half cells at 100 mA g⁻¹. (b) Charge-discharge curves of the **1a@GO//NCM111** full-cell at 100 mA g⁻¹. (c) Cycling performance for **1a@GO//NCM111** full-cell.

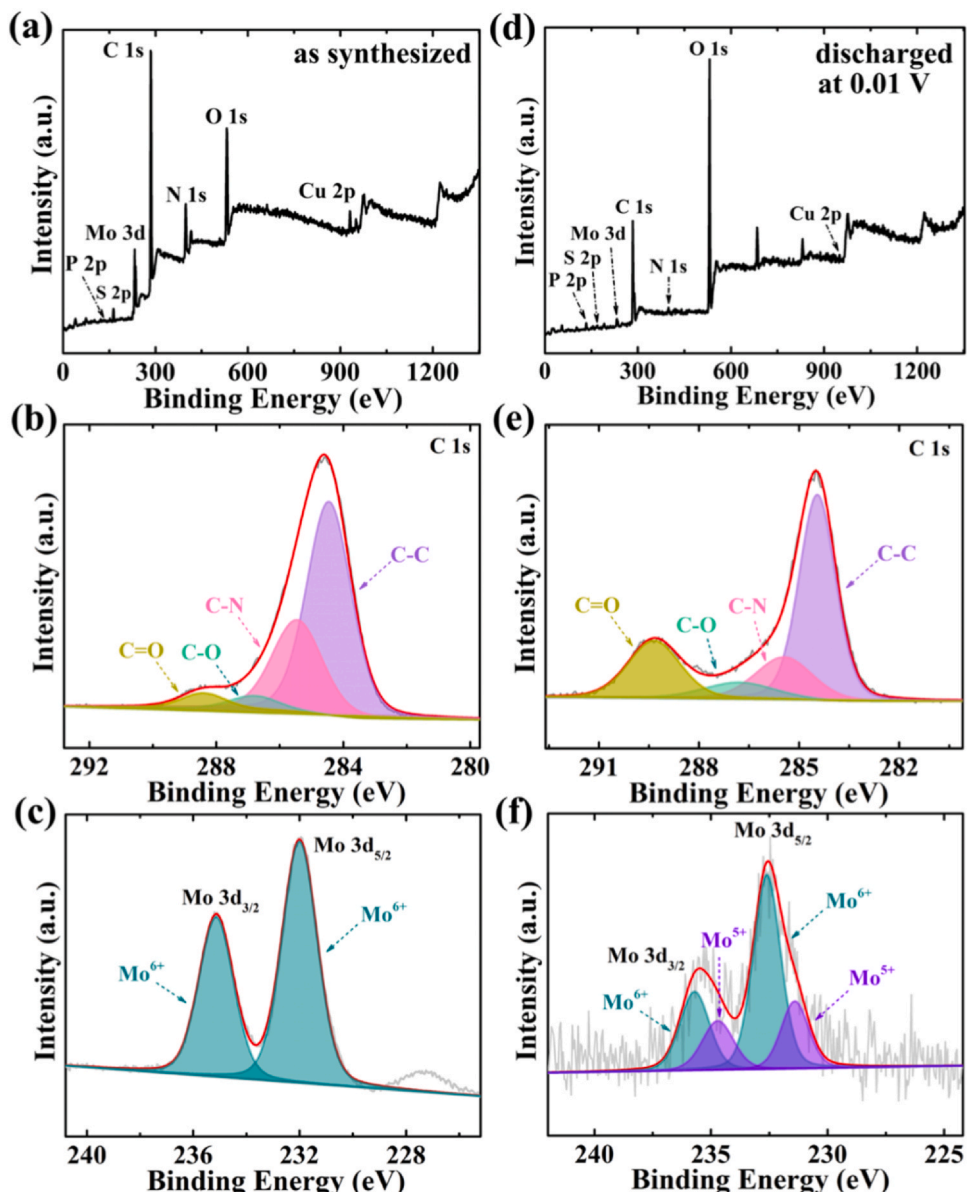


Fig. 11. XPS analysis of **1a** before test and after discharge at 0.01 V. (a) Survey XPS spectrum, (b) high-resolution XPS spectra of C 1s, (c) Mo 3d for the as-synthesized sample, (d) survey XPS spectrum after discharge at 0.01 V for **1a**, (e) high-resolution XPS spectra of C 1s and (f) Mo 3d.

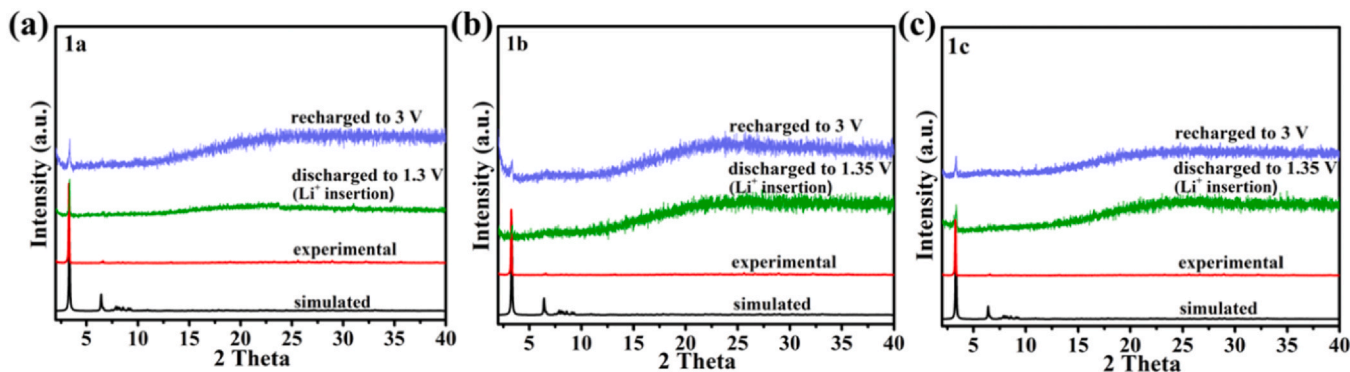


Fig. 12. Ex-situ PXRD patterns of **1a–1c** for the simulated, the as-synthesized, the discharged to 1.3 V or 1.35 V, and the recharged to 3.0 V.

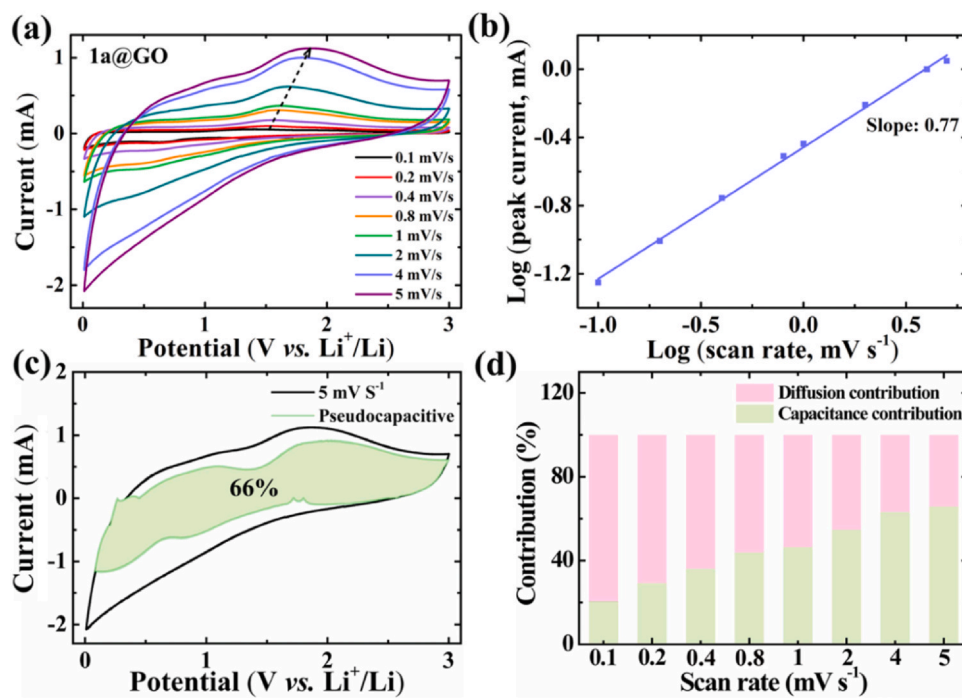


Fig. 13. (a) CV profiles of **1a@GO** with different scan rates (0.1–5 mV/s). (b) Cathodic peak plot of **1a@GO** from log (i_p) to log (v). (c) Capacitance contribution for **1a@GO** (scan rate: 5 mV/s). (d) Capacitance contribution for **1a@GO** with different scan rates (0.1–5 mV/s).

1c@GO, respectively (Figs. 13c, S18c and S19c), enhanced by 46% relative to the ones at 0.1 mV/s (Fig. 13d, S18d and S19d).

3. Conclusions

We have designed a series of stable POM-resorcin[4]arene-based metal–organic complexes with different Keggin-type POMs. Through the ball-milling synthetic method, the redox **Cu-POMs** complexes were successfully incorporated into the conductive RGO to give **Cu-POMs@GO** composites. Significantly, the obtained **Cu-POMs@GO** composites exhibit remarkable electrochemical performance as anode materials of LIBs. This work presented a feasible synthetic strategy for constructing **Cu-POMs** and **Cu-POMs@GO**. The significant improvement of the electrochemical performance for the resulting **Cu-POMs@GO** composites provide the meaningful guidance for the application of POM-based metal–organic complexes as anode materials of LIBs.

CRediT authorship contribution statement

This work was completed through contributions of all authors.

Declaration of Competing Interest

The authors declare that they have no known competing financial interests or personal relationships that could have appeared to influence the work reported in this paper.

Acknowledgments

This work was financially supported by the National Natural Science Foundation of China (Grant 21471029).

Appendix A. Supporting information

Supplementary data associated with this article can be found in the online version at doi:[10.1016/j.jallcom.2021.159009](https://doi.org/10.1016/j.jallcom.2021.159009).

References

- [1] N. Chen, Y. Dai, Y. Xing, L. Wang, C. Guo, R. Chen, S. Guo, F. Wu, Biomimetic antennae ionogel electrolyte boosts the performance of dendrite-free lithium batteries, *Energy Environ. Sci.* 10 (2017) 1660–1667.
- [2] X. Zhang, Y. Yang, Z. Zhou, Towards practical lithium–metal anodes, *Chem. Soc. Rev.* 49 (2020) 3040–3071.
- [3] Q. Huang, K. Turcheniuk, X. Ren, A. Magasinski, A.-Y. Song, Y. Xiao, D. Kim, G. Yushin, Cycle stability of conversion-type iron fluoride lithium battery cathode at elevated temperatures in polymer electrolyte composites, *Nat. Mater.* 18 (2019) 1343–1349.
- [4] F. Wu, V. Srot, S. Chen, S. Lorger, P.A. van Aken, J. Maier, Y. Yu, 3D honeycomb architecture enables a high-rate and long-life iron (III) fluoride–lithium battery, *Adv. Mater.* 31 (2019) 1905146.
- [5] X.-Y. Yang, T. Wei, J.-S. Li, N. Sheng, P.-P. Zhu, J.-Q. Sha, T. Wang, Y.-Q. Lan, Polyoxometalate-incorporated metallapillararene/metallacalixarene metal–organic frameworks as anode materials for lithium ion batteries, *Inorg. Chem.* 56 (2017) 8311–8318.
- [6] Z. Zheng, H.-H. Wu, H. Liu, Q. Zhang, X. He, S. Yu, V. Petrova, J. Feng, R. Kostecki, P. Liu, D.-L. Peng, M. Liu, M.-S. Wang, Achieving fast and durable lithium storage through amorphous FeP nanoparticles encapsulated in ultrathin 3D P-doped porous carbon nanosheets, *ACS Nano* 14 (2020) 9545–9561.
- [7] J. Xu, J. Mahmood, Y. Dou, S. Dou, F. Li, L. Dai, J.-B. Baek, 2D frameworks of C₂N and C₃N as new anode materials for lithium-ion batteries, *Adv. Mater.* 29 (2017) 1702007.
- [8] Y.-T. Weng, H.-W. Liu, A. Pei, F. Shi, H. Wang, C.-Y. Lin, S.-S. Huang, L.-Y. Su, J.-P. Hsu, C.-C. Fang, Y. Cui, N.-L. Wu, An ultrathin ionomer interphase for high efficiency lithium anode in carbonate based electrolyte, *Nat. Commun.* 10 (2019) 5824.
- [9] C. Xu, Z. Liu, T. Wei, L. Sheng, L. Zhang, L. Chen, Q. Zhou, Z. Jiang, L. Wang, Z. Fan, Mesoporous single-crystalline MnO_x nanofibers@graphene for ultra-high rate and long-life lithium-ion battery anodes, *J. Mater. Chem. A* 6 (2018) 24756–24766.
- [10] Y. Luo, D. Huang, C. Liang, P. Wang, K. Han, B. Wu, F. Cao, L. Mai, H. Chen, Fe₂VO₄ hierarchical porous microparticles prepared via a facile surface solvation treatment for high-performance lithium and sodium storage, *Small* 15 (2019) 1804706.
- [11] J. Hua, F. Jia, Y.-F. Song, Engineering high-performance polyoxometalate/PANI/MWNTs nanocomposite anode materials for lithium ion batteries, *Chem. Eng. J.* 326 (2017) 273–280.

- [12] K. Sun, H. Li, H. Ye, F. Jiang, H. Zhu, J. Yin, 3D-structured polyoxometalate microcrystals with enhanced rate capability and cycle stability for lithium-ion storage, *ACS Appl. Mater. Interfaces* 10 (2018) 18657–18664.
- [13] H. İlbeygi, I.Y. Kim, M.G. Kim, W. Cha, P.S.M. Kumar, D.-H. Park, A. Vinu, Highly crystalline mesoporous phosphotungstic acid: a high performance electrode material for energy storage applications, *Angew. Chem. Int. Ed.* 58 (2019) 10849–10854.
- [14] J.-H. Liu, M.-Y. Yu, J. Yang, Y.-Y. Liu, J.-F. Ma, Polyoxometalate-based complex/graphene for high-rate lithium-ion batteries, *Microporous Mesoporous Mater.* 310 (2021) 110666.
- [15] X. Chen, Z. Wang, R. Zhang, L. Xu, D. Sun, A novel polyoxometalate-based hybrid containing a 2D $[\text{CoMo}_8\text{O}_{26}]_\infty$ structure as the anode for lithium-ion batteries, *Chem. Commun.* 53 (2017) 10560–10563.
- [16] H. Wang, S. Hamanaka, Y. Nishimoto, S. Irle, T. Yokoyama, H. Yoshikawa, K. Awaga, In operando X-ray absorption fine structure studies of polyoxometalate molecular cluster batteries: polyoxometalates as electron sponges, *J. Am. Chem. Soc.* 134 (2012) 4918–4924.
- [17] J.-J. Chen, M.D. Symes, S.-C. Fan, M.-S. Zheng, H.N. Miras, Q.-F. Dong, L. Cronin, High-performance polyoxometalate-based cathode materials for rechargeable lithium-ion batteries, *Adv. Mater.* 27 (2015) 4649–4654.
- [18] Y.-H. Ding, J. Peng, S.-U. Khan, Y. Yuan, A new polyoxometalate (POM)-based composite: fabrication through POM-assisted polymerization of dopamine and properties as anode materials for high-performance lithium-ion batteries, *Chem. Eur. J.* 23 (2017) 10338–10343.
- [19] S. Omwoma, C.T. Gore, Y. Ji, C. Hu, Y.-F. Song, Environmentally benign polyoxometalate materials, *Coord. Chem. Rev.* 286 (2015) 17–29.
- [20] Q. Huang, T. Wei, M. Zhang, L.-Z. Dong, A.-M. Zhang, S.-L. Li, W.-J. Liu, J. Liu, Y.-Q. Lan, A highly stable polyoxometalate-based metal–organic framework with π - π stacking for enhancing lithium ion battery performance, *J. Mater. Chem. A* 5 (2017) 8477–8483.
- [21] D. Chai, C.J. Gómez-García, B. Li, H. Pang, H. Ma, X. Wang, L. Tan, Polyoxometalate-based metal–organic frameworks for boosting electrochemical capacitor performance, *Chem. Eng. J.* 373 (2019) 587–597.
- [22] R. Yu, X.-F. Kuang, X.-Y. Wu, C.-Z. Lu, J.P. Donahue, Stabilization and immobilization of polyoxometalates in porous coordination polymers through host–guest interactions, *Coord. Chem. Rev.* 253 (2009) 2872–2890.
- [23] I.V. Kozhevnikov, Catalysis by heteropoly acids and multicomponent polyoxometalates in liquid-phase reactions, *Chem. Rev.* 98 (1998) 171–198.
- [24] P.-P. Zhu, N. Sheng, M.-T. Li, J.-S. Li, G.-D. Liu, X.-Y. Yang, J.-Q. Sha, M.-L. Zhu, J. Jiang, Fabrication and electrochemical performance of unprecedented POM-based metal–carbene frameworks, *J. Mater. Chem. A* 5 (2017) 17920–17925.
- [25] M. Genovese, K. Lian, Ionic liquid-derived imidazolium cation linkers for the layer-by-layer assembly of polyoxometalate–MWNT composite electrodes with high power capability, *ACS Appl. Mater. Interfaces* 8 (2016) 19100–19109.
- [26] F. Xiao, J. Hao, J. Zhang, C. Lv, P. Yin, L. Wang, Y. Wei, Polyoxometalatocyclophanes: controlled assembly of polyoxometalate-based chiral metallamacrocycles from achiral building blocks, *J. Am. Chem. Soc.* 132 (2010) 5956–5957.
- [27] C.T. Buru, P. Li, B.L. Mehdii, A. Dohnalkova, A.E. Platero-Prats, N.D. Browning, K.W. Chapman, J.T. Hupp, O.K. Farha, Adsorption of a catalytically accessible polyoxometalate in a mesoporous channel-type metal–organic framework, *Chem. Mater.* 29 (2017) 5174–5181.
- [28] H.N. Miras, L. Vila-Nadal, L. Cronin, Polyoxometalate based open-frameworks (POM-OFs), *Chem. Soc. Rev.* 43 (2014) 5679–5699.
- [29] H. Ma, B. Liu, B. Li, L. Zhang, Y.G. Li, H.Q. Tan, H.Y. Zang, G. Zhu, Cationic covalent organic frameworks: a simple platform of anionic exchange for porosity tuning and proton conduction, *J. Am. Chem. Soc.* 138 (2016) 5897–5903.
- [30] G. Paille, M. Gomez-Mingot, C. Roch-Marchal, B. Lassalle-Kaiser, P. Mialane, M. Fontecave, C. Mellot-Draznieks, A. Dolbecq, A fully noble metal-free photosystem based on cobalt–polyoxometalates immobilized in a porphyrinic metal–organic framework for water oxidation, *J. Am. Chem. Soc.* 140 (2018) 3613–3618.
- [31] W. Salomon, C. Roch-Marchal, P. Mialane, P. Rouschmeyer, C. Serre, M. Haouas, F. Taulelle, S. Yang, L. Ruhmann, A. Dolbecq, Immobilization of polyoxometalates in the Zr-based metal organic framework UiO-67, *Chem. Commun.* 51 (2015) 2972–2975.
- [32] S.-T. Zhang, J. Yang, H. Wu, Y.-Y. Liu, J.-F. Ma, Systematic investigation of high-sensitivity luminescent sensing for polyoxometalates and iron(III) by MOFs assembled with a new resorcin[4]arene-functionalized tetracarboxylate, *Chem. Eur. J.* 21 (2015) 15806–15819.
- [33] B.-B. Lu, W. Jiang, J. Yang, Y.-Y. Liu, J.-F. Ma, Resorcin[4]arene-based microporous metal–organic framework as an efficient catalyst for CO_2 cycloaddition with epoxides and highly selective luminescent sensing of $\text{Cr}_2\text{O}_7^{2-}$, *ACS Appl. Mater. Interfaces* 9 (2017) 39441–39449.
- [34] W.-Y. Pei, G.H. Xu, J. Yang, H. Wu, B.L. Chen, W. Zhou, J.-F. Ma, Versatile assembly of metal-coordinated calix[4]resorcinarene cavitands and cages through ancillary linker tuning, *J. Am. Chem. Soc.* 139 (2017) 7648–7656.
- [35] W. Jiang, J. Yang, Y.-Y. Liu, S.Y. Song, J.-F. Ma, A stable porphyrin-based porous metal–organic framework as an efficient solvent-free catalyst for C–C bond formation, *Inorg. Chem.* 56 (2017) 3036–3043.
- [36] B.-B. Lu, J. Yang, G.-B. Che, W.-Y. Pei, J.-F. Ma, Highly stable copper(I)-based metal–organic framework assembled with resorcin[4]arene and polyoxometalate for efficient heterogeneous catalysis of azide–alkyne “click” reaction, *ACS Appl. Mater. Interfaces* 10 (2018) 2628–2636.
- [37] X.-X. Wang, J. Yang, X. Xu, J.-F. Ma, Highly stable copper(I)-thiacalix[4]arene-based frameworks for highly efficient catalysis of click reactions in water, *Chem. Eur. J.* 25 (2019) 16660–16667.
- [38] T.-T. Guo, D.-M. Cheng, J. Yang, X. Xu, J.-F. Ma, Calix[4]resorcinarene-based $[\text{Co}_{16}]$ coordination cages mediated by isomorphous auxiliary ligands for enhanced proton conduction, *Chem. Commun.* 55 (2019) 6277–6280.
- [39] T.-T. Guo, X.-F. Su, X. Xu, J. Yang, L.-K. Yan, J.-F. Ma, A calix[4]resorcinarene-based $[\text{Co}_{12}]$ coordination cage for highly efficient cycloaddition of CO_2 to epoxides, *Inorg. Chem.* 58 (2019) 16518–16523.
- [40] M.-Y. Yu, T.-T. Guo, X.-C. Shi, J. Yang, X. Xu, J.-F. Ma, Polyoxometalate-bridged Cu(I)- and Ag(I)-thiacalix[4]arene dimers for heterogeneous catalytic oxidative desulfurization and azide–alkyne “click” reaction, *Inorg. Chem.* 58 (2019) 11010–11019.
- [41] M.-Y. Yu, J. Yang, T.-T. Guo, J.-F. Ma, Efficient catalytic oxidative desulfurization toward thioether and sulfur mustard stimulant by polyoxomolybdate–resorcin [4]arene-based metal–organic materials, *Inorg. Chem.* 59 (2020) 4985–4994.
- [42] W.-Y. Pei, J. Yang, H. Wu, W. Zhou, Y.-W. Yang, J.-F. Ma, A calix[4]resorcinarene-based giant coordination cage: controlled assembly and iodine uptake, *Chem. Commun.* 56 (2020) 2491–2494.
- [43] D. Liu, B.-B. Lu, W.-Y. Pei, Z.-Y. Gu, J. Yang, X.-L. Wu, J.-F. Ma, A new polyoxometalate–resorcin[4]arene-based framework as an efficient anode material for lithium-ion batteries, *J. Alloy. Compd.* 835 (2020) 155314.
- [44] Y. Zheng, S. Zheng, H. Xue, H. Pang, Metal–organic frameworks/graphene-based materials: preparations and applications, *Adv. Funct. Mater.* 28 (2018) 1804950.
- [45] H. Wu, W. Zhang, S. Kandambeth, O. Shekhab, M. Eddaudi, H.N. Alsharif, Conductive metal–organic frameworks selectively grown on laser-scribed graphene for electrochemical microsupercapacitors, *Adv. Energy Mater.* 9 (2019) 1900482.
- [46] T. Wei, M. Zhang, P. Wu, Y.-J. Tang, S.-L. Li, F.-C. Shen, X.-L. Wang, X.-P. Zhou, Y.-Q. Lan, POM-based metal–organic framework/reduced graphene oxide nanocomposites with hybrid behavior of battery-supercapacitor for superior lithium storage, *Nano Energy* 34 (2017) 205–214.
- [47] C. Li, X. Lou, Q. Yang, Y. Zou, B. Hu, Remarkable improvement in the lithium storage property of $\text{Co}_2(\text{OH})_2\text{BDC}$ MOF by covalent stitching to graphene and the redox chemistry boosted by delocalized electron spins, *Chem. Eng. J.* 326 (2017) 1000–1008.
- [48] J. Sun, A. Klechikov, C. Moise, M. Prodana, M. Enachescu, A.V. Talyzin, A molecular pillar approach to grow vertical covalent organic framework nanosheets on graphene: hybrid materials for energy storage, *Angew. Chem. Int. Ed.* 57 (2018) 1034–1038.
- [49] K. Jayaramulu, D.P. Dubal, A. Schneemann, V. Ranc, C. Perez-Reyes, J. Stráská, Š. Kment, M. Otyepka, R.A. Fischer, R. Zboril, Shape-assisted 2D MOF/graphene derived hybrids as exceptional Lithium-ion battery electrodes, *Adv. Funct. Mater.* 29 (2019) 1902539.
- [50] J. Hu, H. Diao, W. Luo, Y.-F. Song, Dawson-type polyoxomolybdate anions ($\text{P}_2\text{Mo}_{18}\text{O}_{62}^{6-}$) captured by ionic liquid on graphene oxide as high-capacity anode material for lithium-ion batteries, *Chem. Eur. J.* 23 (2017) 8729–8735.
- [51] A.L. Spek, PLATONSQUEEZE: a tool for the calculation of the disordered solvent contribution to the calculated structure factors, *Acta Crystallogr. Sect. C Struct. Chem.* 71 (2015) 9–18.
- [52] P. Xiao, F. Bu, R. Zhao, M.F. Aly Aboud, I. Shakir, Y. Xu, Sub-5 nm ultrasmall metal–organic framework nanocrystals for highly efficient electrochemical energy storage, *ACS Nano* 12 (2018) 3947–3953.
- [53] C. Dong, L. Xu, Cobalt- and cadmium-based metal–organic frameworks as high performance anodes for sodium ion batteries and lithium ion batteries, *ACS Appl. Mater. Interfaces* 9 (2017) 7160–7168.
- [54] D. Fu, H. Li, X.-M. Zhang, G. Han, H. Zhou, Y. Chang, Flexible solid-state supercapacitor fabricated by metal–organic framework/graphene oxide hybrid interconnected with PEDOT, *Mater. Chem. Phys.* 179 (2016) 166–173.
- [55] K. Vasanth Kumar, C. Valenzuela-Calahorro, J.M. Juarez, M. Molina-Sabiova, J. Silvestre-Albero, F. Rodriguez-Reinoso, Hybrid isotherms for adsorption and capillary condensation of N_2 at 77 K on porous and non-porous materials, *Chem. Eng. J.* 162 (2010) 424–429.
- [56] P. Sharma, N. Kumar, R. Chauhan, V. Singh, V.C. Srivastava, R. Bhatnagar, Growth of hierarchical ZnO nano flower on large functionalized rGO sheet for superior photocatalytic mineralization of antibiotic, *Chem. Eng. J.* 392 (2020) 123746.
- [57] J.-Q. Sha, X.-Y. Yang, Y. Chen, P.-P. Zhu, Y.-F. Song, J. Jiang, Fabrication and electrochemical performance of polyoxometalate-based three-dimensional metal organic frameworks containing carbene nanocages, *ACS Appl. Mater. Interfaces* 10 (2018) 16660–16665.
- [58] J. Sha, P. Zhu, X. Yang, X. Li, X. Li, M. Yue, K. Zhou, Polyoxometalates templated metal Ag–carbene frameworks anodic material for lithium-ion batteries, *Inorg. Chem.* 56 (2017) 11998–12002.
- [59] Y. Jin, C. Zhao, Z. Sun, Y. Lin, L. Chen, D. Wang, C. Shen, Facile synthesis of Fe-MOF/RGO and its application as a high performance anode in lithium-ion batteries, *RSC Adv.* 6 (2016) 30763–30768.
- [60] Y.-Y. Wang, M. Zhang, S.-L. Li, S.-R. Zhang, W. Xie, J.-S. Qin, Z.-M. Su, Y.-Q. Lan, Diamondoid-structured polymolybdate-based metal–organic frameworks as high-capacity anodes for lithium-ion batteries, *Chem. Commun.* 53 (2017) 5204–5207.
- [61] D. Li, D. Yang, X. Yang, Y. Wang, Z. Guo, Y. Xia, S. Sun, S. Guo, Double-helix structure in carrageenan–metal hydrogels: a general approach to porous metal sulfides/carbon aerogels with excellent sodium-ion storage, *Angew. Chem. Int. Ed.* 55 (2016) 15925–15928.
- [62] D. Wu, H. Li, R. Li, Y. Hu, X. Hu, In situ growth of copper rhodizonate complexes on reduced graphene oxide for high-performance organic lithium-ion batteries, *Chem. Commun.* 54 (2018) 11415–11418.
- [63] R.R. Kapaev, S. Olthof, I.S. Zhidkov, E.Z. Kurmaev, K.J. Stevenson, K. Meerholz, P.A. Troshin, Nickel(II) and copper(II) coordination polymers derived from 1,2,4,5-tetraaminobenzene for lithium-ion batteries, *Chem. Mater.* 31 (2019) 5197–5205.

- [64] J. Xie, Y. Zhang, Y. Han, C. Li, High-capacity molecular scale conversion anode enabled by hybridizing cluster-type framework of high loading with amino-functionalized graphene, *ACS Nano* 10 (2016) 5304–5313.
- [65] M. Govindhan, B. Mao, A. Chen, Novel cobalt quantum dot/graphene nanocomposites as highly efficient electrocatalysts for water splitting, *Nanoscale* 8 (2016) 1485–1492.
- [66] J.-S. Qin, D.-Y. Du, W. Guan, X.-J. Bo, Y.-F. Li, L.-P. Guo, Z.-M. Su, Y.-Y. Wang, Y.-Q. Lan, H.-C. Zhou, Ultrastable polymolybdate-based metal–organic frameworks as highly active electrocatalysts for hydrogen generation from water, *J. Am. Chem. Soc.* 137 (2015) 7169–7177.
- [67] W. Cheng, F.-C. Shen, Y.-S. Xue, X. Luo, M. Fang, Y.-Q. Lan, Y. Xu, A pair of rare three-dimensional chiral polyoxometalate-based metal–organic framework enantiomers featuring superior performance as the anode of lithium-ion battery, *ACS Appl. Energy Mater.* 1 (2018) 4931–4938.
- [68] M.-T. Li, X.-Y. Yang, J.-S. Li, N. Sheng, G.-D. Liu, J.-Q. Sha, Y.-Q. Lan, Assembly of multifold helical polyoxometalate-based metal–organic frameworks as anode materials in lithium-ion batteries, *Inorg. Chem.* 57 (2018) 3865–3872.
- [69] H. Hosseini, S. Shahrokhian, Self-supported nanoporous Zn–Ni–Co/Cu selenides microball arrays for hybrid energy storage and electrocatalytic water/urea splitting, *Chem. Eng. J.* 375 (2019) 122090.
- [70] J. Sun, J. Liu, H. Chen, X. Han, Y. Wu, J. He, C. Han, G. Yang, Y. Shan, Strongly coupled Mo₂C and Ni nanoparticles with in-situ formed interfaces encapsulated by porous carbon nanofibers for efficient hydrogen evolution reaction under alkaline conditions, *J. Colloid Interface Sci.* 558 (2020) 100–105.